Title

Wake vortex regimes of a pitching cantilever plate in quiescent air and their correlation with mean flow generation

Authors

Ebrahimi, Navid Dehdari
Eldredge, Jeff D
Ju, Y Sungtaek

Publication Date

2019

DOI

10.1016/j.jfluidstructs.2018.11.010

Peer reviewed

Wake vortex regimes of a pitching cantilever plate in quiescent air and their correlation with mean flow generation

Navid Dehdari Ebrahimi*, Jeff D. Eldredge, Y. Sungtaek Ju
Department of Mechanical and Aerospace Engineering, University of California, Los Angeles, CA 90095, USA

Abstract- Jet flows induced by oscillating cantilever plates enable power-efficient cooling enhancement and fluid acceleration. We report a combined experimental and numerical study of the vortex regimes present in the wake of a harmonically oscillating thin cantilever plate in a quiescent fluid and analyze their effect on the flow generation downstream. We use Particle Image Velocimetry (PIV) in conjunction with two-dimensional numerical simulations to investigate the vortex evolution around the trailing edge of the plates with different geometries and vibrational properties. Our observations suggest the existence of three distinct regimes in the wake: non-propagating, intermediate and propagating. Comparing the temporal decay of the vortex circulation in different regimes shows that different mechanisms are involved in the formation of these vortical patterns. A regime map is proposed next, denoting the incident of each vortex regime as a function of relevant dimensionless parameters. Our analysis of the mean jet on the normal mid-plane, as quantified by the momentum-averaged Reynolds number Re_{jet}, shows that the induced jet downstream the trailing edge is tightly correlated with the identified vortex regimes. The present study improves our understanding of vortex generation and propagation in oscillating cantilevers and facilitates optimized design and operation of piezoelectric fans and similar devices.

Keywords: flapping wing, jet flows, oscillating cantilevers, piezoelectric fans, pitching plate, vortex regime

I. Introduction

Interactions between vibrating cantilever plates and surrounding fluids have been the subject of many studies. These structures have continued to gain attention due to a variety of applications, such as piezoelectric fans for electronics cooling [1]–[3], electrostatic [4] and electromagnetic [5] fluid accelerators, energy harvesting using vortex induced vibrations [6]–[8], micro air vehicles (MAVs) [9], ionic polymer metal composites (IPMCs) [10]–[13], and micro-mixers and aerosol collectors [14]. Applications that require net flow generation, such as piezoelectric fans, rely primarily on vortex generation at the trailing edges. Understanding the mechanisms and patterns of vortex generation and propagation is critical for the systematic design and optimization of vibrating plates in these applications.

Vortex shedding around submerged oscillating objects was studied in classic investigations of vibrating cylinders in water [15]–[17]. These studies revealed different vortex regimes in the wake of a cylinder at different vibration frequencies and amplitudes and examined their impact on the drag and lift forces. Koochesfahani [18] and Bohl *et al.* [19] reported vortical patterns resulting from sinusoidal and non-sinusoidal pitching airfoils under varying free stream conditions. They observed that changes from negative (drag) to positive (thrust) force coefficients or from velocity deficit to velocity excess occur at specific frequencies and amplitudes that nearly correspond to changes in vortex patterns. Similarly, Schnipper *et al.* [20] experimentally demonstrated different vortex patterns in the wake of a pitching airfoil in a uniform free stream flow and reported a phase diagram in the dimensionless frequency and amplitude space. In an attempt to model idealized fish caudal fins (tail), Green *et al.* [21] studied the unsteady three-dimensional wake vortices produced by a pitching trapezoidal panel in varying freestream velocities. They observed thrust-producing vortex alignment in the vicinity of the normal mid-plane and drag-producing vortices closer to the edges. Buchholz *et al.* [22]–[24] investigated the wake structure of a series of low-aspect-ratio pitching plates in a non-zero freestream environment and found that with decreasing the aspect ratio or increasing the Strouhal number, the vortex pattern in the wake changes from 2S to 2P, where two pairs of vortices are shed in each cycle. These studies, however, cannot be generalized to vibrating cantilever plates

operating in air, such as piezoelectric fans, which involve zero freestream velocity and operate at higher Reynolds numbers.

Lai [25] studied a plunging airfoil in quiescent water, but no observations on associated vortex patterns were reported. Heathcote *et al.* [26] examined flexible flapping beams in a quiescent fluid to analyze the effect of the beam amplitude and stiffness on the thrust generation. This study was again performed at low Reynolds numbers and the vibration amplitudes at the leading edge were comparable with those at the trailing edge. In their numerical study of IPMC vibrating cantilevers in water, Abdelnour *et al.* [12] qualitatively observed that in low Reynolds flows, vorticity is confined in the vicinity of the cantilever tip and dissipates with a fast rate, whereas at higher Reynolds numbers, vorticity can travel a relatively longer distance before dissipation. They also concluded that the observed trends in the vorticity generation and convection are highly correlated with thrust production in vibrating cantilevers. This study, however, did not conduct a comprehensive investigation of the observed vortex patterns and their correlation with thrust production.

Kim *et. al.* [27]–[30] studied flow fields generated by vibrating flat beams in air both numerically using the moving mesh method and experimentally using the PIV and smoke visualization techniques. These results helped elucidate the mechanisms of vortex generation and transport, but only a single frequency and a narrow range of amplitudes were considered. In fact, as we shall show later, for the particular frequency used, the transition band between different vortical regimes is narrow and thus, difficult to capture. Eastman *et al.* [31] studied the thrust force generation by vibrating cantilever plates and proposed a correlation between the thrust and the vibration amplitude and frequency. The frequency range used in this study, however, was again rather narrow (59 – 63 Hz).

Shrestha *et al.* [32] proposed a 2D vortex regime map for a vibrating cantilever plate in the dimensionless frequency and amplitude domain. This past study was, however, concerned with flows generated from the lateral sides of a vibrating cantilever plate, as opposed to the downstream of its trailing edge, because the primary focus of the study was the relation between aerodynamic drag forces and observed vortex patterns. The reported results were also limited to a cantilever plate of a fixed geometry.

In the present manuscript, we investigate flow regimes for thin cantilever plates of systematically varied geometries, resonant frequencies and amplitudes oscillating in quiescent air and examine their correlation with downstream flow generation. We perform particle imaging velocimetry (PIV) experiments together with numerical simulation based on the immersed boundary method (IBM) to characterize vortex generation and propagation and to compare the temporal decays of vortices generated in different regimes. Downstream flows are characterized in terms of the momentum-averaged velocity and associated jet Reynolds number.

The rest of the paper is organized as follows. In Sec.II we describe the parameters and experimental setup used in the present study. Sec.III provides the detailed description of the geometry, time-space discretization, solver properties and validity of the numerical simulations reported in this study. Sec.IV contains the results and discussions regarding the vortex patterns observed in the experiments and numerical studies. Summary and conclusions are presented in Sec.V.

II. Experiment Parameters and Setup

The vibration characteristics of the cantilevers are described by their frequency, f, and amplitude, A. The tip characteristic velocity is given as $u_{tip} = fA$. The main length scale in the problem is the length of the cantilever, L_c. The aspect ratio, w_c/L_c, and the thickness of the plates only have secondary effects on the vortex generation and propagation along the centerline. We introduce two independent dimensionless parameters: a normalized amplitude, α and an oscillatory Reynolds number for the cantilever, Re_c:

$$\alpha = \frac{A}{L_c} \textbf{ Error! Bookmark not defined.} \quad (1)$$

$$Re_c = \frac{u_{tip}\, L_c}{\nu} = \frac{f\, A\, L_c}{\nu} \tag{2}$$

where ν is the kinematic viscosity of the fluid. We refer to Re_c simply as the Reynolds number throughout the rest of the paper. It is sometimes convenient to remove the amplitude in one of the dimensionless parameters. This can be done by using the ratio Re_c/α

$$\frac{Re_c}{\alpha} = \frac{f\, {L_c}^2}{\nu} \tag{3}$$

As we are dealing with oscillating plates in an otherwise quiescent fluid, the Strouhal number cannot be defined.

A piezoelectric actuator (Steminc Inc., SMPF61W20F50) is employed in the present study to oscillate cantilevers at their resonance frequencies. The piezoelectric actuator consists of two 185 μm-thick piezoelectric ceramic films (Pb ($Zr_{0.53}Ti_{0.47}$) O_3; PZT-4) and a 142 μm-thick copper shim sandwiched in between. It is 20 mm wide and 23 mm long (Fig. 1a). Flexible blades of different materials and geometries are made in-house and attached to the actuator using cyanoacrylate glue. Table I lists the geometric parameters of the blades along with the resonance frequencies, *f*, and the ranges of vibrational amplitudes, *A*, used in the present study.

A function generator (Model 33220A, Agilent) is used to generate sinusoidal voltage waves of amplitude 0.05 V – 2 V, which are then amplified by a factor of 100 using a high-voltage amplifier (Model PZD700A, TREK) before being fed to the actuator (Fig.1c). The vibration amplitudes are measured optically with an uncertainty of approximately 10 μm, less than 5% of the minimum amplitude used in this study. Different resonance frequencies for the same cantilever are obtained by changing the mass distribution using a method reported in a previous study [33]. We verified that the different cantilevers used exhibit similar modal shapes at different frequencies (Fig.1b).

The PIV setup (Fig.1c) comprises a 500 mW continuous wave laser (Hercules, LASERGLOW Technologies) with a wavelength of 532 nm. The laser beam is shaped into a light sheet using a cylindrical lens (plano-concave lens, f = -3.9 mm, ThorLabs). We use a high-speed camera (Phantom VEO-640L) capable of recording 16-bit, 4-megapixel images to capture the motion of particles suspended in the air. The frame rate is chosen such that at least 100 frames are captured per full period of the oscillations. A shutter speed of 80 μs is considered adequate for eliminating the effects of motion blur in these experiments.

PIV experiments are conducted in a sealed box made of transparent acrylic plates (30 cm × 20 cm × 8 cm), large enough to reduce interference from the side walls [34]. Seeding particles are generated by heating a solution of water and glycerin (30% glycerin in volume). They are allowed to settle for about a minute before conducting any recording to minimize initial disturbance from previous experiments. The particle motions due to buoyancy are measured separately in the absence of an oscillating plate and deducted from velocity fields.

An open-source software package [35], [36] is used to analyze the captured video images. This software utilizes the Advanced Discrete Fourier Transform technique in which smaller sub areas of two successive frames are cross-correlated to obtain the direction and magnitude of particles' displacements in the sub-areas. The calculated velocity fields are next post-processed by manually filtering the outlier data and replacing them with interpolated equivalents in areas where improper lighting condition leads to inaccurate displacement vectors. An algorithm based on penalized least squares method [37] is employed to reduce the noise in the flow fields.

The PIV setup and image processing procedure are validated using several benchmarks in [38]. An uncertainty of 0.14 pixel is estimated for the displacement vectors, which translates into an uncertainty in velocity of 0.016 m/s in our experiments.

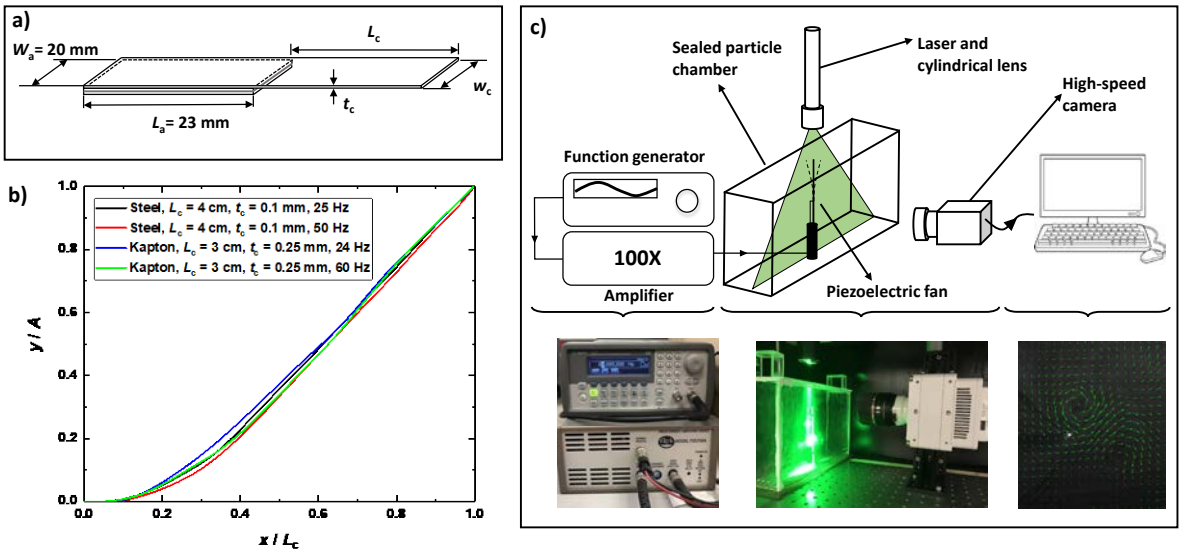

Fig. 1. (a) Schematic of the piezoelectric actuator and the attached blade, forming a vibrating cantilever plate (b) normalized modal shape of the cantilevers with blades of different materials and resonance frequencies (c) schematic of the PIV visualization setup.

Table I. Characteristics of the cantilevers used in the experiments and the corresponding oscillatory Reynolds numbers R_c.

Material	t_c (mm)	L_c (mm)	w_c (mm)	f (Hz)	A (mm)	$Re_c = L_c f A/\nu$
steel	0.1	15	30	90	0.18 - 2	16 - 172
	0.1	15**	30	155**	0.26 - 2.5	39 – 371
Kapton	0.127	20	30	72	0.3 - 4.6	28 – 422
	0.127	20	30	96	0.5 - 2	61 – 245
	0.127	30*	30	20*	0.3 - 3.6	11 – 138
	0.127	30	30	29	0.3 - 3.9	17 – 216
	0.127	30**	30	39**	0.3 - 4.2	22 – 313
polyester	0.03	20	30	21	0.5 - 2.9	13 – 78
	0.03	20	30	30	0.4 - 3	15.3 - 114
	0.03	20*	30	45*	0.5 - 3.6	29 - 207

III. Numerical Simulations

We perform two-dimensional numerical simulations using a commercial computational fluid dynamics package (Ansys CFX) to help interpret our experimental results. We use the Immersed Boundary Method [39] to avoid computational overheads associated with re-meshing in moving mesh methods. Table II summarizes the flow conditions simulated. The flow field generated downstream of an oscillating cantilever plate is inherently three-dimensional and more complex than can be captured in a two-dimensional simulation [21], [30], [40]–[42]. However, the velocity field and vortex generation on the mid-plane normal to the cantilever (Fig. 2a) can be approximated as two dimensional [27].

Table II. Conditions used in numerical simulation

L_c (mm)	f (Hz)	A (mm)	$Re_c = L_c f A/\nu$
20	45	0.3 - 3.5	17 – 201
20	21	0.5 - 3.5	13 – 94
30	29	0.3 - 3.7	17 – 205
30	39	0.3 - 3.2	22 – 239

The simulation domain is chosen to be of size $3L_c \times L_c$ based on our experimental observations, such that it is large enough to capture vortex propagation while avoiding any complicating effect at the boundaries. To help resolve the details of vortex propagation, we use meshes of spatially varying sizes: $0.005L_c$ in a circle of a radius of $0.25L_c$ around the cantilever tip, $0.01L_c$ in an intermediate circle with a radius of $0.45L_c$, and $0.025L_c$ in the rest of the domain (Fig.2b). To confirm mesh independence, a representative case is run 10 full cycles to reach stable flows [29] using different mesh sizes. Halving the mesh sizes from the chosen values results in less than 5% changes in the peak and average velocities at mid-points between two successive vortices propagating downstream while increasing the run time from 40 minutes to 50 hours on a workstation (Intel® Xeon® 2.30 GHz, 32 GB RAM).

An open boundary condition is specified on the outer walls of the simulation domain (Fig.2a). This boundary condition allows fluid motion in both directions normal to the boundary. The relative pressure on the walls is specified as zero. The deformation of the cantilever plate is approximated as an immersed solid prescribed to rotate rigidly about a pivot point at its base; this simplification is justified by the predominance of the lowest-order vibration mode (see Fig.1b). Our approximation is also reasonable because there is no incident flow from upstream to be affected by the details of the plate mounting. We also would like to emphasize that it is the motion at the trailing edge and its vicinity that are most important for establishing the wake profile and its thrust or drag signature. This is inherent, for example, in the asymptotic approach known as local interaction theory, in which the behavior of the boundary layers approaching the trailing edge is reconciled with the near wake. This led to a number of papers that espoused a “triple-deck” structure to reconcile these two regions (see [43]). Furthermore, in Lighthill’s elongated body theory in aquatic propulsion (see for instance [44]), all of the momentum generated by the intermediate motion along the body is canceled by reciprocal motions, except at the trailing edge.

The first-order upwind scheme is used for advection terms and the second-order backward Euler scheme is used in time to discretize the governing equations. For each numerical simulation, the time step is chosen such that the Courant number remains lower than one in computational cells.

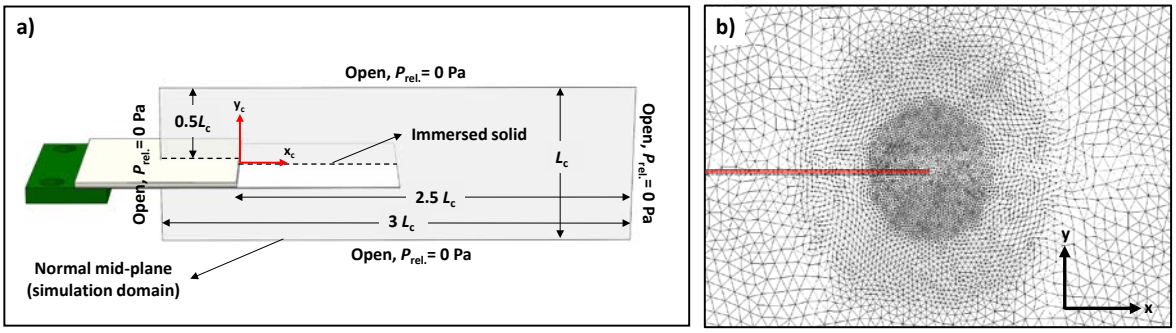

Fig. 2. (a) Simulation domain (b) typical mesh used in the present study (images are not to scale).

IV. Results

In pitching airfoils and oscillating cantilever plates, the entire vorticity originates in the boundary layer due to the no slip condition. In the presence of an external flow, the non-zero free stream modulates the development of the boundary layer and can facilitate vortex shedding from the leading edge or mid-body besides the trailing edge. The frequency of vortex shedding in this case is influenced by the free stream velocity and can be different from the frequency of the oscillations, creating complex vortex patterns in the wake of the oscillator (up to 16 vortices in a period at high freestream velocity and low oscillation frequencies reported in [20]). This mechanism is absent without the free stream and the frequency of vortex shedding is the same as the frequency of the oscillations, f. As a result, only two counter-rotating vortices in each cycle are shed from the trailing edge [27], [45]. Our observations from the PIV experiments identify three distinct regimes of vortex generation and propagation in the wake of an oscillating flat plate.

Non-propagating vortex regime

At low Reynolds numbers ($Re_c < 37$), counter-rotating vortices are generated at the tip during each cycle: a clockwise vortex in the up stroke and a counter-clockwise vortex in the down stroke. The vortices remain attached to the cantilever in this regime and do not propagate downstream. Each of these counter-rotating vortices lasts only approximately half a cycle and disappears with the generation of a next vortex. Only a single vortex is effectively visible at a given instant. Fig.3 shows the time sequence of vortex formation in a representative PIV experiment, and Fig.4 depicts the corresponding numerical simulation results.

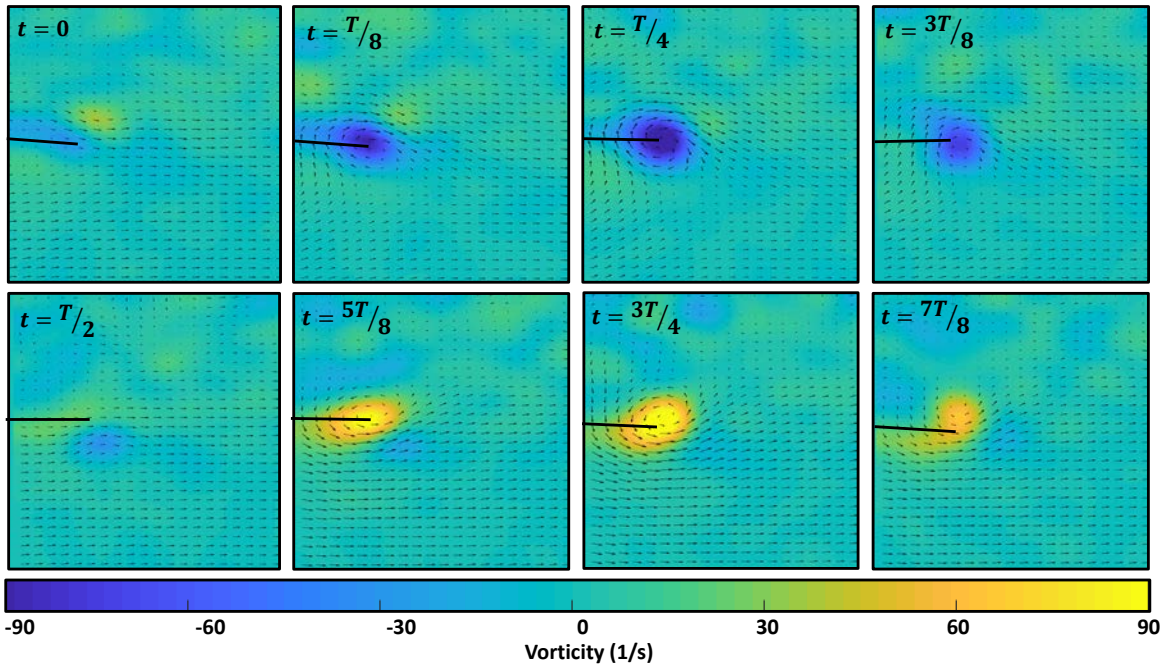

Fig. 3. The time sequence of vortex generation and evolution over a full cycle for a representative case in the non-propagating regime: $Re_c = 25.12$ and $\alpha = 0.015$ ($L_c = 30$ mm, $f = 39$ Hz, $A = 0.453$ mm)

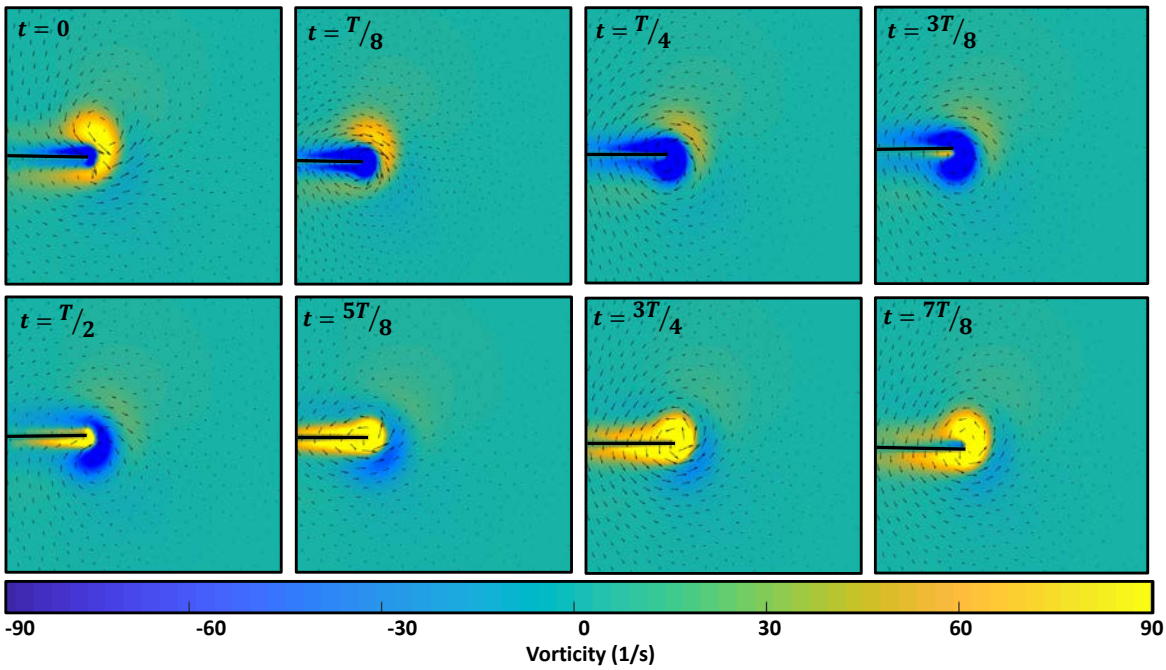

Fig. 4. The time sequence of vortex generation and evolution obtained from numerical simulation under the conditions of the experiment shown in Fig. 3.

Our PIV experiments and numerical simulation show that, in this regime, forward flow generation due to a vortex attached on one side of the plate is essentially canceled out by reverse flow generation on the other side of the plate, leading to a negligible mean jet. The fluid motion along the length of the cantilever is essentially just upward or downward, and the velocity component in the forward direction is negligible. This is somewhat reminiscent of the flow regime observed by Shrestha *et al.* [32], where isolated attached vortices are observed at low amplitudes and frequencies with no significant convection on the lateral side of a vibrating cantilever. We previously observed poor performance of piezoelectric fans operating in this regime [46]. A similar behavior was reported in [47] for a piezoelectric fan operating at low amplitudes, where the so-called viscous streaming flows are created on the top and bottom of a thin oscillating plate.

Intermediate vortex regime

At moderate Reynolds numbers ($37 < Re_c < 70$), we observe a transitioning behavior, that is, vortices detach from the cantilever tip and propagate downstream. In this regime, a forward flow generated on one side of the plate overcomes a reverse flow generated on the opposite side, resulting in a net forward flow. The detached vortices, however, have low strength and their fast dissipation makes them very susceptible to deformation by subsequently generated vortices, significantly tilting the induced flow and limiting its spatial range. Due to the rapid dissipation of the vortices generated, two fully detached vortex are not observed at the same time. Figs. 5 and 6 show the sequence of vortex shedding in this regime obtained from the PIV experiments and numerical simulation.

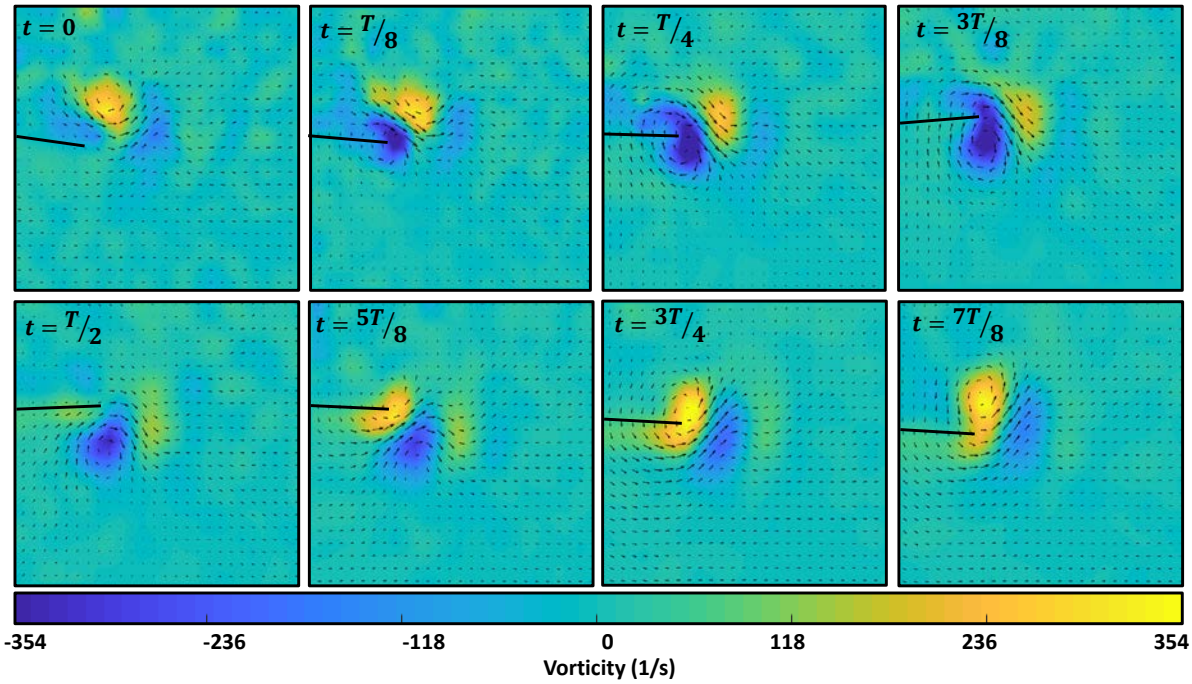

Fig. 5. The time sequence of vortex generation and evolution over a full cycle for a representative experiment in the intermediate regime: Re_c = 37.43 and α = 0.022 (L_c = 30 mm, f = 29 Hz, A = 0.675 mm)

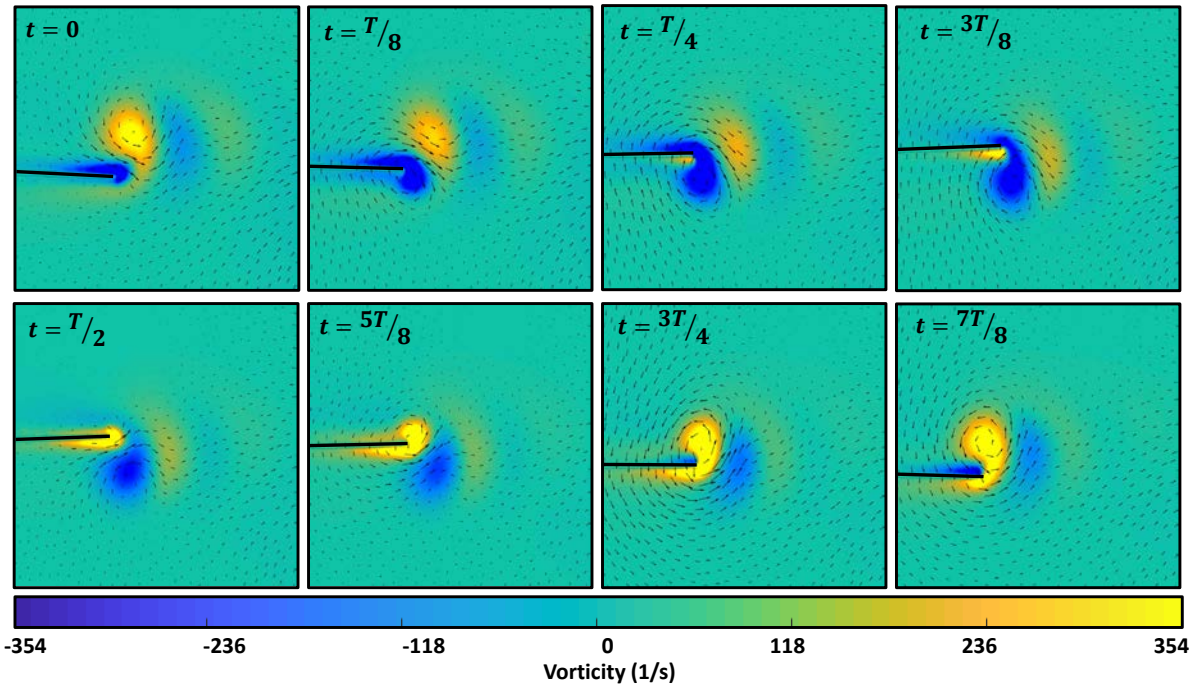

Fig. 6. The time sequence of vortex generation and evolution obtained from numerical simulation corresponding to the conditions of the experiment shown in Fig. 5.

Propagating vortex regime

At still higher Reynolds numbers (Re_c > 70), we observe propagating vortices. In contrast to the intermediate regime, a vortex generated in this regime does not dissipate as completely after a half cycle and thus two counter-rotating vortices are observed propagating downstream. Figs. 7 and 8 illustrate the vortex generation and propagation in this regime. Contrary to the non-propagating regime, the propagating vortices move completely to one side of the plate immediately upon creation. The forward velocity component on one side of a new vortex is augmented by its preceding vortex, and a high-velocity region is created in the space between the two adjacent vortices as they move downstream. These vortices resemble a thrust producing inverse Von Kármán vortex street observed in the wake of a pitching airfoil in [18], [20].

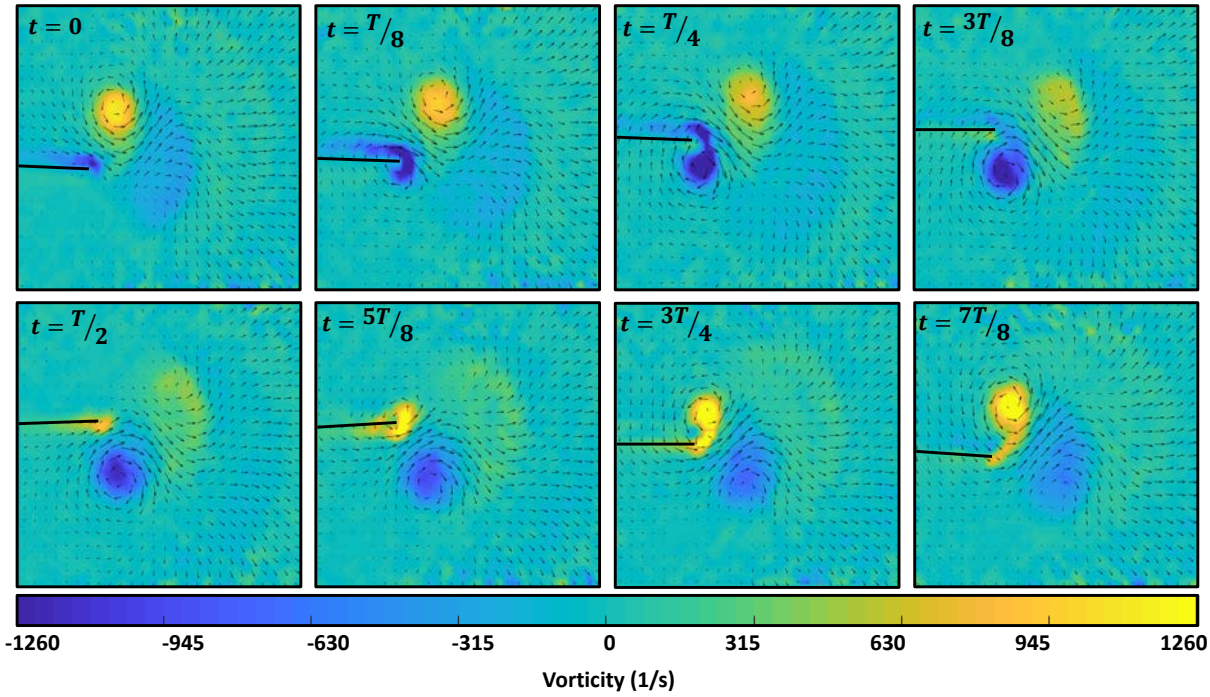

Fig. 7. The time sequence of vortex generation and evolution over a full cycle for a representative experiment in the propagating regime: Re_c = 87 and α = 0.039 (L_c = 30 mm, f = 39 Hz, A = 1.2 mm)

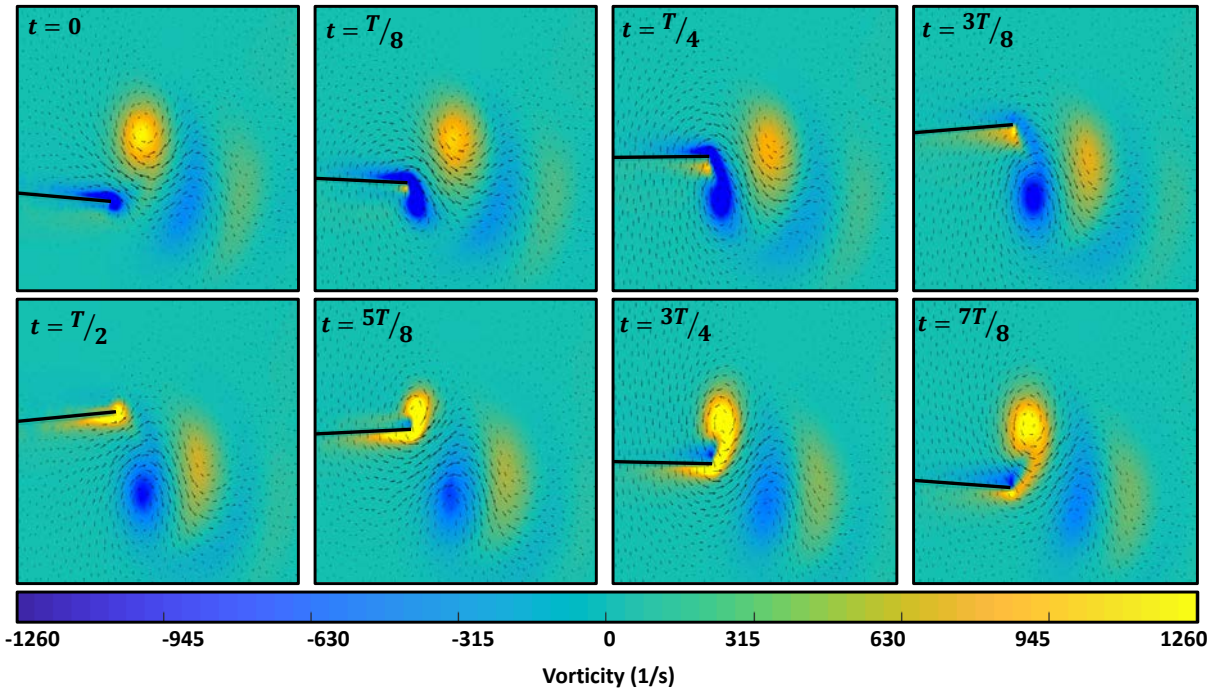

Fig. 8. The time sequence of vortex generation and evolution obtained from numerical simulation under the conditions of the experiment shown in Fig. 7.

To further investigate vortex evolution in different regimes, we plot the ratio $\Gamma(t)/\Gamma_{max}$ as a function of the normalized time t/T for a counter-clockwise vortex (Fig. 9a). Here, $\Gamma(t)$ is the circulation contained in the vortex core at time t, measured using the area integral of the vorticity in the vortex core, and Γ_{max} is the maximum circulation in a full cycle. The vortex core in a 2D flow field is identified using an algorithm reported in Graftieaux *et al.* [48]. The experimental results reported by Kim *et al.* [27] are also shown in the graph for comparison. In their work, the propagating regime at higher Reynolds numbers (Re_c ~ 400) was investigated.

Fig. 9a shows that for all the cases investigated here, the vortex generation starts slightly earlier than the beginning of the vibration cycle. The circulation then increases almost linearly and peaks at t/T~ 0.25, approximately when the tip passes its neutral position. After this point, the circulation contained in the vortex core starts to decay. The rate of decay is different for different regimes: the circulation decreases rapidly in the non-propagating regime, approaching nearly zero at half the cycle (t/T~ 0.5), and the vortex effectively dissipates when the next vortex is formed. In the intermediate regime, the circulation decays immediately after reaching the peak, but at a lower rate. The circulation drops by approximately 40% at half the cycle and reaches 30% of its peak strength by the time a subsequent clock-wise vortex reaches its maximum circulation (t/T~ 0.75). In the propagating regime, the circulation remains approximately constant after reaching the peak until it begins to gradually decrease at t/T~ 0.5 - 0.6.

We can attribute the high decay rates in the non-propagating and intermediate regimes to vorticity annihilation, that is, the succession of oppositely-signed vortices canceling each other. This effect is more pronounced for these regimes because each generated vortex does not travel far from a subsequently generated vortex. Conversely, in the propagating regime, vorticity annihilation is less effective as vortices are further separated from each other. As a result, vortices are mostly influenced by vorticity diffusion rather than annihilation in the propagating regime. For a two-dimensional vortex in the presence of diffusion, such as Lamb – Oseen, the strength of the vortex core remains approximately constant because the core radius and the vorticity diffusion scale similarly with time (~ $t^{1/2}$) [49]. This explains the flatness

of the temporal profiles of $\Gamma(t)$ after the peak in the propagating regime. The circulation does decrease as a subsequent oppositely-signed vortex catches up eventually.

For flow conditions well within the non-propagating or propagating regime, the temporal circulation decay exhibits nearly universal behavior and is approximately independent of Re_c (the red symbols/curves and the blue symbols/curves in Fig. 9a). In contrast, as the flow condition approaches and crosses the non-propagating regime boundary ($Re_c \sim 37$), we observe rapid changes in the circulation decay curves as the Reynolds number is increased.

To help quantitatively compare the relative abruptness in these changes, we define the approximate linear decay rate of the normalized circulation. This decay rate is obtained as the negative slope of a fit to an approximately linear portion of each circulation decay curve from Fig. 9a at $t/T \geq 0.3$. Fig. 9b illustrates the normalized decay rate thus obtained as a function of Re_c. Additional numerical simulations were performed right near the regime boundaries.

Figure 9b shows that the approximate linear decay rate is nearly constant away from the first regime boundary ($Re_c << 37$). It then decreases rapidly as the flow condition approaches and then crosses this regime boundary. Once the flow condition enters the intermediate regime, the approximate linear decay rate decreases much more gradually with increasing Reynolds numbers. We remind the reader that the intermediate regime does not represent a distinct primary flow regime, but rather a transition band within which hybrid vortical behavior and flow characteristics are observed. In the intermediate regime, vortices detach and propagate from the trailing edge but dissipate rather quickly. As we approach the boundary between the intermediate and propagating regimes ($Re_c \sim 70$), the decay rate once again undergoes more rapid changes but not as rapid as near the first regime boundary ($Re_c \sim 37$). For flow conditions well within the propagating regime ($Re_c >> 70$), the linear decay rate is approximately constant at a small value.

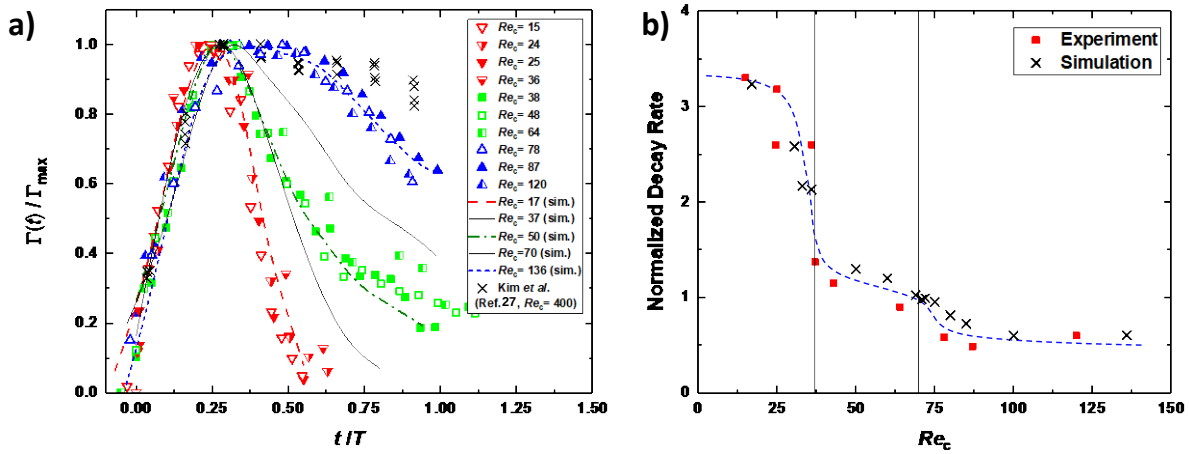

Fig. 9. a) Normalized circulation in a cycle of oscillations. The data corresponding to regime boundaries are indicated by solid black lines. b) Approximate linear decay rate of the normalized circulation as a function of Re_c. The blue dashed line is a guide to the eye. The solid vertical lines correspond to the regime boundaries (Re_c = 37, 70).

Average velocity profiles and streamlines

The evolution of the vortices generated at the tip of a cantilever governs the velocity profile downstream of the cantilever plate. Figs.10a - 10c show the velocity profiles averaged over one cycle for each regime along with the associated streamlines.

In the non-propagating regime (Fig.10a), the absence of vortex shedding and the presence of a single vortex at each half cycle results in a weak and short-range net flow generation in the forward direction. In the intermediate regime (Fig.10b), the forward velocity is increased. In propagating regime (Fig.10c), the presence of two vortices leads to a high-velocity region in the middle as the two counter-rotating vortices augment each other.

The curvature of the streamlines and their concentration in front of the cantilever is another indicator of the influence of vortex shedding on the surrounding fluid. Facci *et al*. [42] used the orientation and curvature of the streamlines at different cross-sections of their cantilever plates to investigate the aerodynamics loads in their three dimensional numerical simulations. As illustrated in Fig.10a, the streamlines in the non-propagating regime are barely deformed and the streamlines in front of the plate are sparse compared with the other two cases. The transitioning nature of the intermediate regime can be recognized from the deformation of the streamlines around the cantilever tip in Fig.10b, where the streamlines tend to form closed loops. In contrast, the streamlines around the tip of the cantilever form concentric lines under the influence of the propagating vortices in Fig. 10c.We believe that the slight asymmetry observed in Fig.10 is caused by imperfections in the cantilever plates, such as slight misalignment in the mounting or built-in bias in cantilever deflections. These were also considered in [27], [50] as potential reasons for asymmetric velocity profiles in front of the cantilever.

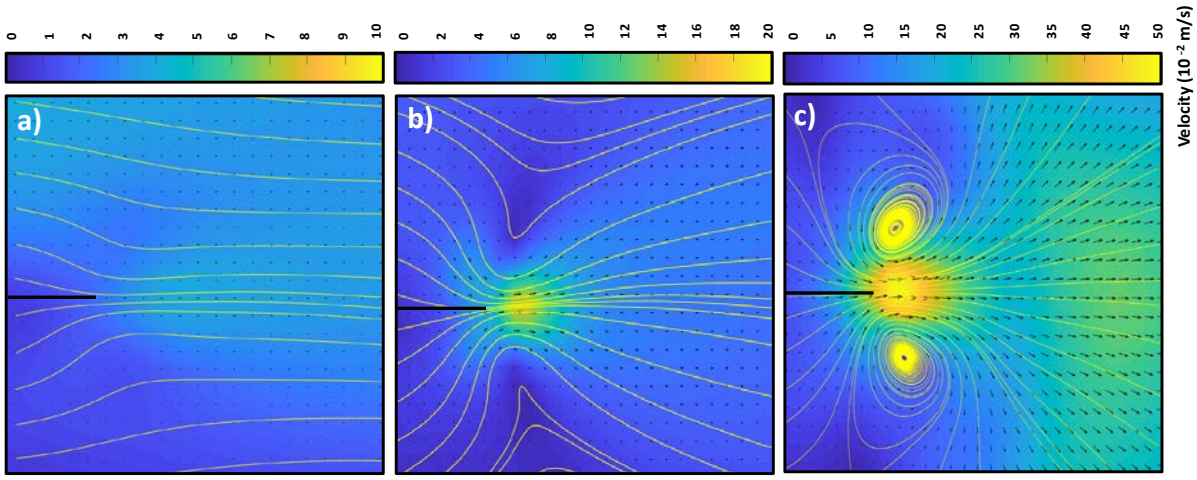

Fig. 10. The average velocity field obtained from PIV experiments over one period of vibration and the corresponding stream lines for (a) the non-propagating (b) the intermediate and (c) the propagating regime shown in Figs. 3, 5 and 7, respectively. The velocity vectors have the same scale in the figures.

Regime map and correlation with airflow generation

We construct the vortex regime map in the (α, Re_c/α) plane ($0 < \alpha < 0.2$ and $500 < Re_c/\alpha < 2500$) by systematically increasing the vibration amplitude while observing the resulting flow patterns. Corresponding results from our numerical simulations are also shown, but with a slight shift to the right to avoid overlap.

For each value of Re_c/α, the vortex pattern starts in the non-propagating regime. As the value of α is increased (corresponding to moving up in the regime map), the vortices start to detach from the cantilever tip and form the intermediate vortex pattern described earlier. As Fig.11 suggests, this transition band is wider for smaller Re_c/α and narrower at larger Re_c/α. Increasing α further past the transition band, we observe the propagating vortex patterns. Two sets of data for $Re_c/\alpha = 1150$ and $Re_c/\alpha = 2200$ are obtained using different combinations of geometric and vibrational parameters indicated by * and ** in table I. The vortex patterns observed in the numerical simulations agree well with the experiments. Our results show that the transition band is confined between the lines of constant Re_c ($Re_c = 37$ and $Re_c = 70$). The lines of constant Re_c were also observed to demark transition between the von Kármán and reverse von Kármán vortex regime in a previous study [20]. More specifically, they observed that the transition from von Kármán to reverse von Kármán in a non-zero freestream velocity medium around a pitching airfoil takes place at a constant tip characteristic velocity Af for a fixed cord length. Shrestha *et al*. [32] reported a critical

value of $Re_c \sim 21$ for the transition from the symmetric to asymmetric vortex regime for the lateral vortex generation of a submerged flat cantilever plate in water.

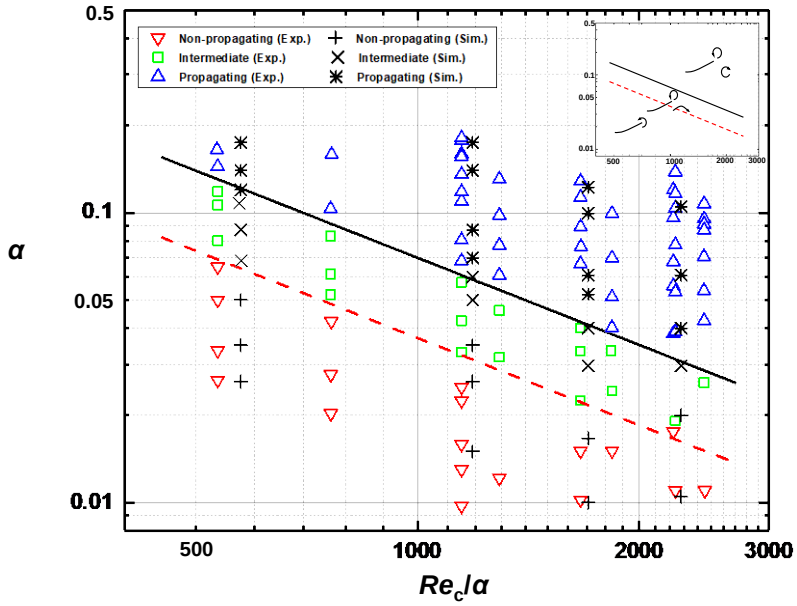

Fig. 11. The vortex regime map. Separating lines of constant Re_c are shown with dashed (corresponding to $Re_c = 37$) and solid (corresponding to $Re_c = 70$) lines. Simulation data points are shown with a slight shift to the right to avoid overlap.

In many applications, such as cooling enhancement using piezoelectric fans, the average flow generation in the streamwise direction due to the cantilever vibrations is of great interest. To investigate the effect of the observed vortex patterns on downstream flow generation capability, we define a Reynolds number associated with the produced jet, Re_{jet}, as

$$Re_{jet} = \frac{\bar{u}_m A}{\nu} \tag{4}$$

where $\bar{u}_m$ is the momentum-averaged velocity of the jet, calculated from

$$\bar{u}_m = \left(\frac{\int_{-\infty}^{+\infty} (u(x_c,y))^2 \, dy}{2A} \right)^{\frac{1}{2}} \tag{5}$$

Here, $u(x_c,y)$ is the velocity profile in front of the cantilever tip at $x = x_c$. Fig. 12a schematically shows the procedure to obtain Re_{jet}. The location at which the velocity profile is taken has a minor influence on Re_{jet} because the fluid momentum is conserved along the x direction. In fact, our experimental results show that Re_{jet} remains essentially constant up to a distance equal to $4A$ downstream of the cantilever tip. Fig.12b shows the Re_{jet} obtained from the measured velocity profiles at different locations in front of the cantilever plate for each vortex pattern together with the Re_{jet} obtained from corresponding numerical simulations.

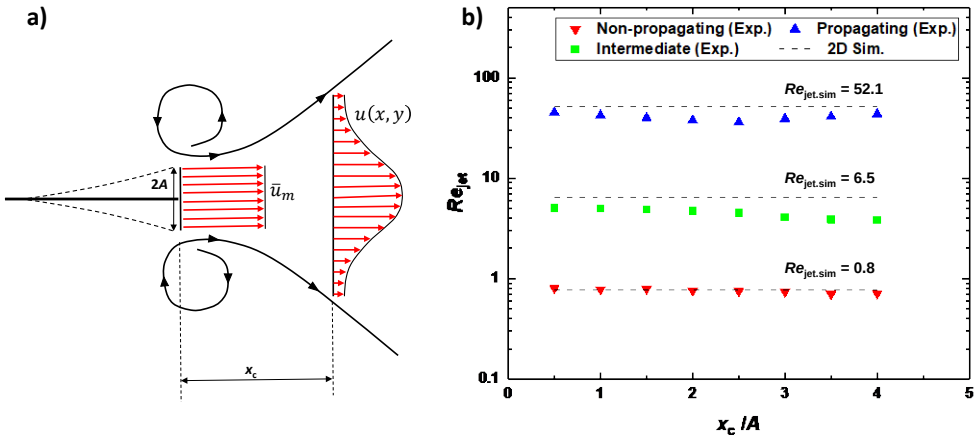

Fig. 12. (a) Schematic illustrating the procedure of obtaining Re_{jet} in front of the cantilever tip (b) Re_{jet} as a function of the distance in the streamwise direction from the cantilever. The symbols and the black dashed lines represent the PIV results and corresponding numerical simulation results, respectively.

Fig. 13 shows Re_{jet} as a function of Re_c. The different regimes are represented in different colors. In the propagating regime (blue), Re_{jet} increases almost linearly with Re_c with a slope of ~ 0.8. The non-propagating regime (red) shows a weaker dependence on Re_c, with a slope of ~ 0.1. These trends are consistent with the fact that vortex propagation is critical for long-range net forward flow generation. We indeed observed a precipitous drop in the performance of piezoelectric fans operating in the non-propagating regime [46]. These fans had a relatively high power consumption due to increased dielectric and hysteresis losses at high frequencies, but poor heat transfer performance as a result of weak net forward flow generation. Data in the intermediate regime do not follow a distinct trend but rather are scattered between the two trend lines. The data presented in this figure are also in-line with the findings of Peterson *et al.* [10], where inappreciable thrust was measured in IPMC cantilevers at Reynolds numbers below 60.

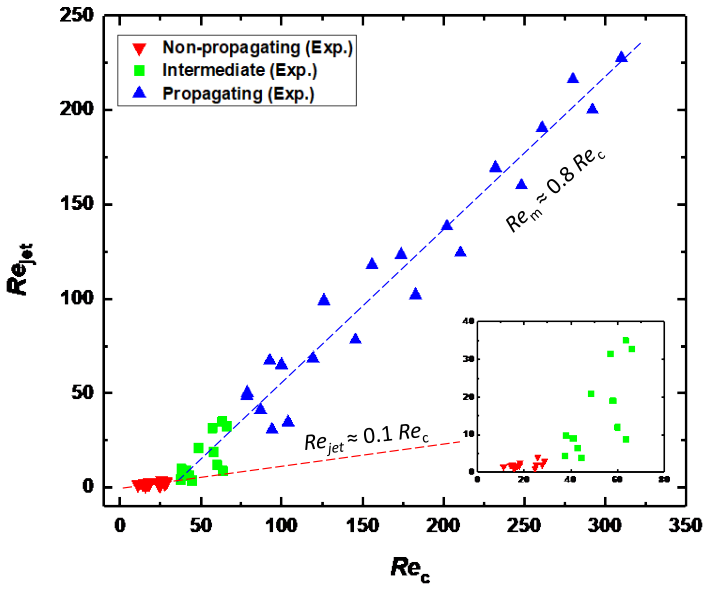

Fig. 13. Jet Reynolds number, Re_{jet}, as a function of the oscillatory Reynolds number, Re_c. The red and blue dashed lines serve as guides to the eye, representing the linear trend of the data points in the non-propagating regime and the propagating regime, respectively.

V. Conclusion

We investigated the vortex regimes present in the wake of a harmonically oscillating cantilever plate in a quiescent, incompressible, viscous fluid and analyzed their effect on the mean fluid jet downstream. More than 100 cantilever plates were examined over a wide range of Reynolds numbers ($10 < Re_c < 300$) using Particle Image Velocimetry and Immersed Boundary numerical simulations. Based on the qualitative features of the vortex shedding from the trailing edge, we identified three distinct vortex regimes in the wake, namely non-propagating, intermediate and propagating. We further demonstrated that these vortical patterns can be presented in a regime map in the parameter space of α and Re_c/α, with lines of constant Re_c as transition lines between adjacent regimes. At low Reynolds numbers ($Re_c < 37$) vortices do not propagate downstream and disappear with the generation of the next vortex (non-propagating regime). Increasing the Reynolds number ($37 < Re_c < 70$) enables the vortices to detach from the trailing edge and propagate downstream. These vortices, however, have low strength and dissipate quickly as the next vortex is formed (intermediate regime). At higher Reynolds numbers ($Re_c > 70$), vortices do not dissipate as completely after a half cycle and thus two counter-rotating vortices are observed propagating downstream. Comparing the temporal decay of the vortex strength in each regime, as quantified by the circulation contained in the vortex core, further revealed that the non-propagating and intermediate vortices are primarily influenced by the destructive effect of the subsequent vortex. This effect is less pronounced for the propagating cases as the vortices are more isolated.

Our qualitative and quantitative analysis of the flow on the normal mid-plane revealed that these vortex regimes significantly affect the mean fluid jet downstream of the thin plate. In the non-propagating regime, Re_{jet} is comparably lower and exhibits a weaker dependency on Re_c ($Re_{jet} \sim 0.1\ Re_c$), suggesting a low flow generation efficiency in this regime. In the propagating regime, Re_{jet} increases almost linearly with Re_c with a slope of ~ 0.8. We did not notice a clear trend for intermediate vortices.

The present study improves our understanding of the vorticity generation and transport in oscillating cantilever plates operating in quiescent fluids. Findings from this study are of significant importance in the applications such as piezoelectric cooling enhancement that highly rely on the airflow generation in front of the cantilever plates. Operation of such devices in non-propagating regime may result in a weak cooling performance and low power efficiency. The novel regime map introduced here provides a useful guide for selecting optimal operating conditions of similar devices.

VI. Acknowledgement

The present article is based in part on work supported by the Advanced Research Projects Agency-Energy (ARPA-E) under Award No. DE-AR0000532.

VII. Declaration of Interest

None.

VIII. References

[1] A. Hales and X. Jiang, “A review of piezoelectric fans for low energy cooling of power electronics,” *Appl. Energy*, vol. 215, pp. 321–337, Apr. 2018.

[2] J. H. Yoo, J. I. Hong, and W. Cao, “Piezoelectric ceramic bimorph coupled to thin metal plate as cooling fan for electronic devices,” *Sens. Actuators Phys.*, vol. 79, no. 1, pp. 8–12, Jan. 2000.

[3] I. Sauciuc *et al.*, “Key challenges for the piezo technology with applications to low form factor thermal solutions,” in *Thermal and Thermomechanical Proceedings 10th Intersociety Conference on Phenomena in Electronics Systems, 2006. ITHERM 2006.*, 2006, p. 5 pp.-pp.785.

[4] H.-C. Wang, N. E. Jewell-Larsen, and A. V. Mamishev, “Thermal management of microelectronics with electrostatic fluid accelerators,” *Appl. Therm. Eng.*, vol. 51, no. 1–2, pp. 190–211, Mar. 2013.
[5] H.-C. Su and H. Y. Xu, “Investigation of a double oscillating-fan cooling device using electromagnetic force,” *Appl. Therm. Eng.*, vol. 103, pp. 553–563, Jun. 2016.
[6] A. L. C. Fujarra, C. P. Pesce, F. Flemming, and C. H. K. Williamson, “VORTEX-INDUCED VIBRATION OF A FLEXIBLE CANTILEVER,” *J. Fluids Struct.*, vol. 15, no. 3, pp. 651–658, Apr. 2001.
[7] T. Sarpkaya, “A critical review of the intrinsic nature of vortex-induced vibrations,” *J. Fluids Struct.*, vol. 19, no. 4, pp. 389–447, May 2004.
[8] C. H. K. Williamson and R. Govardhan, “A brief review of recent results in vortex-induced vibrations,” *J. Wind Eng. Ind. Aerodyn.*, vol. 96, no. 6, pp. 713–735, Jun. 2008.
[9] N. Gravish, J. M. Peters, S. A. Combes, and R. J. Wood, “Collective Flow Enhancement by Tandem Flapping Wings,” *Phys. Rev. Lett.*, vol. 115, no. 18, p. 188101, Oct. 2015.
[10] C. Prince, W. Lin, J. Lin, S. D. Peterson, and M. Porfiri, “Temporally-resolved hydrodynamics in the vicinity of a vibrating ionic polymer metal composite,” *J. Appl. Phys.*, vol. 107, no. 9, p. 94908, May 2010.
[11] S. D. Peterson, M. Porfiri, and A. Rovardi, “A Particle Image Velocimetry Study of Vibrating Ionic Polymer Metal Composites in Aqueous Environments,” *IEEEASME Trans. Mechatron.*, vol. 14, no. 4, pp. 474–483, Aug. 2009.
[12] K. Abdelnour, E. Mancia, S. D. Peterson, and M. Porfiri, “Hydrodynamics of underwater propulsors based on ionic polymer–metal composites: a numerical study,” *Smart Mater. Struct.*, vol. 18, no. 8, p. 85006, 2009.
[13] M. Aureli, C. Pagano, and M. Porfiri, “Nonlinear finite amplitude torsional vibrations of cantilevers in viscous fluids,” *J. Appl. Phys.*, vol. 111, no. 12, p. 124915, Jun. 2012.
[14] R. J. Linderman, O. Nilsen, and V. M. Bright, “Electromechanical and fluidic evaluation of the resonant microfan gas pump and aerosol collector,” *Sens. Actuators Phys.*, vol. 118, no. 1, pp. 162–170, Jan. 2005.
[15] G. H. Koopmann, “The vortex wakes of vibrating cylinders at low Reynolds numbers,” *J. Fluid Mech.*, vol. 28, no. 3, pp. 501–512, May 1967.
[16] O. M. Griffin and S. E. Ramberg, “The vortex-street wakes of vibrating cylinders,” *J. Fluid Mech.*, vol. 66, no. 3, pp. 553–576, Nov. 1974.
[17] C. H. K. Williamson and A. Roshko, “Vortex formation in the wake of an oscillating cylinder,” *J. Fluids Struct.*, vol. 2, no. 4, pp. 355–381, Jul. 1988.
[18] M. M. Koochesfahani, “Vortical patterns in the wake of an oscillating airfoil,” *AIAA J.*, vol. 27, no. 9, pp. 1200–1205, 1989.
[19] D. G. Bohl and M. M. Koochesfahani, “MTV measurements of the vortical field in the wake of an airfoil oscillating at high reduced frequency,” *J. Fluid Mech.*, vol. 620, pp. 63–88, Feb. 2009.
[20] T. Schnipper, A. Andersen, and T. Bohr, “Vortex wakes of a flapping foil,” *J. Fluid Mech.*, vol. 633, pp. 411–423, Aug. 2009.
[21] M. A. Green, C. W. Rowley, and A. J. Smits, “The unsteady three-dimensional wake produced by a trapezoidal pitching panel,” *J. Fluid Mech.*, vol. 685, pp. 117–145, Oct. 2011.
[22] J. H. J. Buchholz and A. J. Smits, “The wake structure and thrust performance of a rigid low-aspect-ratio pitching panel,” *J. Fluid Mech.*, vol. 603, pp. 331–365, May 2008.
[23] J. H. J. Buchholz and A. J. Smits, “On the evolution of the wake structure produced by a low-aspect-ratio pitching panel,” *J. Fluid Mech.*, vol. 546, pp. 433–443, Jan. 2006.
[24] J. H. J. Buchholz, M. A. Green, and A. J. Smits, “Scaling the circulation shed by a pitching panel,” *J. Fluid Mech.*, vol. 688, pp. 591–601, Dec. 2011.
[25] J. C. Lai and M. F. Platzer, “Characteristics of a plunging airfoil at zero freestream velocity,” *AIAA J.*, vol. 39, no. 3, pp. 531–534, 2001.
[26] S. Heathcote, D. Martin, and I. Gursul, “Flexible flapping airfoil propulsion at zero freestream velocity,” *AIAA J.*, vol. 42, no. 11, 2004.

[27] Y.-H. Kim, S. T. Wereley, and C.-H. Chun, “Phase-resolved flow field produced by a vibrating cantilever plate between two endplates,” *Phys. Fluids 1994-Present*, vol. 16, no. 1, pp. 145–162, Jan. 2004.
[28] Y.-H. Kim, C. Cierpka, and S. T. Wereley, “Flow field around a vibrating cantilever: coherent structure eduction by continuous wavelet transform and proper orthogonal decomposition,” *J. Fluid Mech.*, vol. 669, pp. 584–606, Feb. 2011.
[29] M. Choi, C. Cierpka, and Y.-H. Kim, “Vortex formation by a vibrating cantilever,” *J. Fluids Struct.*, vol. 31, no. Supplement C, pp. 67–78, May 2012.
[30] M. H. Oh, S. H. Park, Y.-H. Kim, and M. Choi, “3D flow structure around a piezoelectrically oscillating flat plate,” *Eur. J. Mech. - BFluids*, vol. 67, pp. 249–258, Jan. 2018.
[31] A. Eastman, J. Kiefer, and M. Kimber, “Thrust measurements and flow field analysis of a piezoelectrically actuated oscillating cantilever,” *Exp. Fluids*, vol. 53, no. 5, pp. 1533–1543, Sep. 2012.
[32] B. Shrestha, S. N. Ahsan, and M. Aureli, “Experimental study of oscillating plates in viscous fluids: Qualitative and quantitative analysis of the flow physics and hydrodynamic forces,” *Phys. Fluids*, vol. 30, no. 1, p. 13102, Jan. 2018.
[33] N. Dehdari Ebrahimi, Y. Wang, and Y. S. Ju, “Mechanisms of power dissipation in piezoelectric fans and their correlation with convective heat transfer performance,” *Sens. Actuators Phys.*, vol. 272, pp. 242–252, Apr. 2018.
[34] A. Eastman and M. L. Kimber, “Aerodynamic damping of sidewall bounded oscillating cantilevers,” *J. Fluids Struct.*, vol. 51, pp. 148–160, Nov. 2014.
[35] W. Thielicke and E. Stamhuis, “PIVlab – Towards User-friendly, Affordable and Accurate Digital Particle Image Velocimetry in MATLAB,” *J. Open Res. Softw.*, vol. 2, no. 1, Oct. 2014.
[36] W. Thielicke and E. J. Stamhuis, “PIVlab - Time-Resolved Digital Particle Image Velocimetry Tool for MATLAB (version: 1.41).” .
[37] D. Garcia, “Robust smoothing of gridded data in one and higher dimensions with missing values,” *Comput. Stat. Data Anal.*, vol. 54, no. 4, pp. 1167–1178, Apr. 2010.
[38] W. Thielicke, “The flapping flight of birds: Analysis and application,” University of Groningen, 2014.
[39] “Immersed Boundary Methods,” *Annu. Rev. Fluid Mech.*, vol. 37, no. 1, pp. 239–261, 2005.
[40] S. N. Ahsan and M. Aureli, “Three-Dimensional Analysis of Shape-Morphing Cantilever Oscillations in Viscous Fluids,” p. V003T22A005, Oct. 2017.
[41] C.-N. Lin, “Analysis of three-dimensional heat and fluid flow induced by piezoelectric fan,” *Int. J. Heat Mass Transf.*, vol. 55, no. 11–12, pp. 3043–3053, May 2012.
[42] A. L. Facci and M. Porfiri, “Analysis of three-dimensional effects in oscillating cantilevers immersed in viscous fluids,” *J. Fluids Struct.*, vol. 38, no. Supplement C, pp. 205–222, Apr. 2013.
[43] D. G. Crighton, “The Kutta condition in unsteady flow,” *Annu. Rev. Fluid Mech.*, vol. 17, no. 1, pp. 411–445, 1985.
[44] S. J. Lighthill, *Mathematical biofluiddynamics*. SIAM, 1975.
[45] T. Y.-T. Wu, “Swimming of a waving plate,” *J. Fluid Mech.*, vol. 10, no. 3, pp. 321–344, May 1961.
[46] N. Dehdari Ebrahimi, Z. Zeng, and Y. S. Ju, “Vortex propagation in air flows generated by piezoelectric fans and their correlation with fan cooling power efficiency,” *Proc. 16th Int. Heat Transf. Conf. IHTC-16*, to be published.
[47] T. Açıkalın, A. Raman, and S. V. Garimella, “Two-dimensional streaming flows induced by resonating, thin beams,” *J. Acoust. Soc. Am.*, vol. 114, no. 4, pp. 1785–1795, Oct. 2003.
[48] L. Graftieaux, M. Michard, and N. Grosjean, “Combining PIV, POD and vortex identification algorithms for the study of unsteady turbulent swirling flows,” *Meas. Sci. Technol.*, vol. 12, no. 9, p. 1422, 2001.
[49] J.-Z. Wu, H. Ma, and M.-D. Zhou, *Vorticity and Vortex Dynamics*. Springer Science & Business Media, 2007.
[50] M. Choi, C. Cierpka, and Y.-H. Kim, “Vortex formation by a vibrating cantilever,” *J. Fluids Struct.*, vol. 31, pp. 67–78, May 2012.